ROYAL SOCIETY
OF CHEMISTRY

## PAPER

Check for updates

# Scalable copper current collectors with precisely engineered lithiophilic alloy "skins" for durable lithium-metal batteries†

Huiqun Wang,‡[a] Yuxiang Mao,‡[a] Peng Xu,[a] Yu Ding,[a] Huiping Yang,[a] Jian-Feng Li, [iD][a] Yu Gu,*[a] Jiajia Han, [iD]*[b] Li Zhang [iD]*[a] and Bing-Wei Mao [iD][a]

Depositing a uniform lithium metal layer on a highly conductive current collector (CC) is essential for the development of next-generation Li metal batteries (LMBs). However, poor cycling stability, low Coulombic efficiency, and the potential safety hazards associated with Li dendrite growth remain major obstacles to their commercialization. Herein, a lithiophilic copper–zinc ($Cu_{0.64}Zn_{0.36}$) alloy "skin" is fabricated on commercial Cu CCs for LMBs using an adjustable and scalable ultrafast high-temperature (UHT) Joule heating method. The $Cu_{0.64}Zn_{0.36}$ alloy exhibits strong lithiophilicity, facilitating uniform nucleation and growth of Li metal on its surface, thereby enabling dendrite-free deposition. Density functional theory (DFT) and molecular dynamics (MD) simulations further convincingly support the experimental results. Benefiting from these enhancements, this modified Cu CC demonstrates excellent long-term stability in both Li‖Cu half-cells and full-batteries paired with $LiFePO_4$ or $LiNi_{0.9}Co_{0.05}Mn_{0.05}O_2$ cathodes. More importantly, the versatile UHT method can be extended to develop various metal-"skin"-coated CCs, offering an ingenious strategy for creating composite lithiophilic materials. This work presents a viable pathway for the batch production of advanced Cu CCs for high-performance Li anodes, laying a significant foundation for the practical application of high-energy-density LMBs.

### Broader context

Lithium metal batteries (LMBs) are emerging as a leading next-generation energy storage system owing to their exceptional energy density, making them ideal for applications in electric vehicles, portable electronics, and renewable energy storage. Quantitatively pre-depositing lithium onto the current collectors (CCs) as the anode, or even directly using the CCs as the anode to prepare an anode-free LMBs, can not only push the battery's energy density towards the theoretical limit but also minimize production costs. In both configurations, the design and mass production of highly lithiophilic CCs face significant challenges. Our work utilizes ultrafast high-temperature (UHT) Joule heating technology to controllably and mass-produce a lithiophilic copper–zinc ($Cu_{0.64}Zn_{0.36}$) alloy "skin" layer on Cu CCs, enabling the high reversible plating and stripping of ultra-thin lithium layers in both half cells and full batteries. This work will have a broad impact on three levels: First, this method can be extended to the mass production of various metal-"skin"-coated CCs, demonstrating universal applicability. Second, CCs with highly lithiophilic "skins" will greatly advance the application of high-energy-density LMBs. Third, our innovative approach can also provide transformative solutions for current collector modification in other electrochemical energy systems, such as fuel cells and alkali-metal-based batteries.

[a] *College of Chemistry and Chemical Engineering, State Key Laboratory of Physical Chemistry of Solid Surfaces, The MOE Key Laboratory of Spectrochemical Analysis and Instrumentation, Tan Kah Kee Innovation Laboratory, Collaborative Innovation Center of Chemistry for Energy Materials (iChEM), Xiamen University, Xiamen 361005, Fujian, China. E-mail: ygu@xmu.edu.cn, zhangli81@xmu.edu.cn*

[b] *College of Materials, Fujian Key Laboratory of Surface and Interface Engineering for High Performance Materials, Xiamen Key Laboratory of High Performance Metals and Materials, Xiamen University, Xiamen, 361005, Fujian, China. E-mail: jiajiahan@xmu.edu.cn*

† Electronic supplementary information (ESI) available. See DOI: https://doi.org/10.1039/d4ee05862c

‡ H. Q. Wang and Y. X. Mao contribute equally to this work.

## 1. Introduction

Lithium metal batteries (LMBs), with high theoretical energy densities, are considered one of the most promising candidates for next-generation high-energy-density energy storage systems,[1,2] particularly as the continuous advancements in electronic devices and electric vehicles.[3–6] However, the high intrinsic reactivity of Li metal readily induces undesirable side reactions with electrolyte components,[7] causing the dynamic reconfiguration of uneven solid–electrolyte interphase (SEI) as well as Li dendrite growth.[8–12] These dual adverse effects accumulate over time,

**2622** | *Energy Environ. Sci.*, 2025, **18**, 2622–2633

This journal is © The Royal Society of Chemistry 2025

ultimately leading to battery failure. Consequently, developing highly stable Li metal anodes has become a recognized technical challenge.[13,14] To address these challenges, various strategies have been explored, including the use of electrolyte additives,[15–18] the creation of artificial SEIs,[12,19–21] the customization of pulse charge/discharge protocols,[22,23] and the design of Li deposition frameworks.[24–28] While these methods have improved SEI properties and enhanced Li plating-stripping behaviour, issues related to SEI instability and Li dendrite formation remain significant obstacles to the practical application of Li metal anodes. Notably, many approaches require excess Li during battery assembly. For instance, when employing 200% excess Li, the theoretical volumetric capacity of the LMBs drops from 2060 mA h L$^{-1}$ to approximately 690 mA h L$^{-1}$.[29] Furthermore, excess Li metal can lead to performance degradation and safety concerns.[30] Additionally, due to its poor processability, Li foil thinner than 50 μm is prone to damage or contamination during rolling, posing challenges to large-scale production.[31–33]

In recent years, LMBs utilizing a finite amount of pre-deposited Li on the current collectors (CCs) as an anode, and even anode-free LMBs where the CC directly serves as the anode, have been considered optimal solutions for the practical application of LMBs.[34,35] In both configurations, the CC is pivotal in achieving high battery performance.[36,37] Planar Cu foils, known for their excellent conductivity, processability, and stability at low potentials,[38,39] have long been the preferred choice for anode CCs. However, the lattice mismatch between conventional Cu and Li disrupts the nucleation and growth of Li on the surface.[40] This also affects the local current density and Li$^+$ flux distribution, conclusively resulting in Li dendrite growth and low Coulombic efficiency (CE). One effective strategy to mitigate these issues is the introduction of a functional lithiophilic modification layer on the surface of the Cu CCs, which stabilizes Li plating and stripping, thereby enhancing the performance of LMBs.[41–44] Current methods for constructing such modification layers include physical vapor deposition,[45–48] slurry coating,[49–52] chemical immersion,[53–55] and molten injection.[21,56,57] For example, Liu et al. improved the lithiophilicity of Cu CCs by depositing a Cu$_{99}$Zn alloy layer via magnetron sputtering, resulting in better Li deposition behavior.[46] Similarly, Yu et al. applied a single-ion conductor polymer through spin-coating on the Cu surface, achieving uniformity and adhesion, which effectively enhanced the interface stability.[58] Chemical impregnation has also gained attention for its simplicity and ease of operation, while molten Li-containing alloy processes show great promise in forming alloy layers with excellent scalability potential.[57] Despite these advancements, significant challenges remain for large-scale production of reformative Cu CCs with high-quality modification layer. These challenges include poor bonding strength between the modification layer and Cu CCs, low reversibility of Li deposition and dissolution,[14] insufficient long-term stability, harsh preparation conditions, and difficulties in scaling up manufacturing. Therefore, developing a low-cost, highly durable, and scalable process for the batch production of lithiophilic Cu CCs is urgently needed to propel the next generation of ultra-high energy density LMBs.
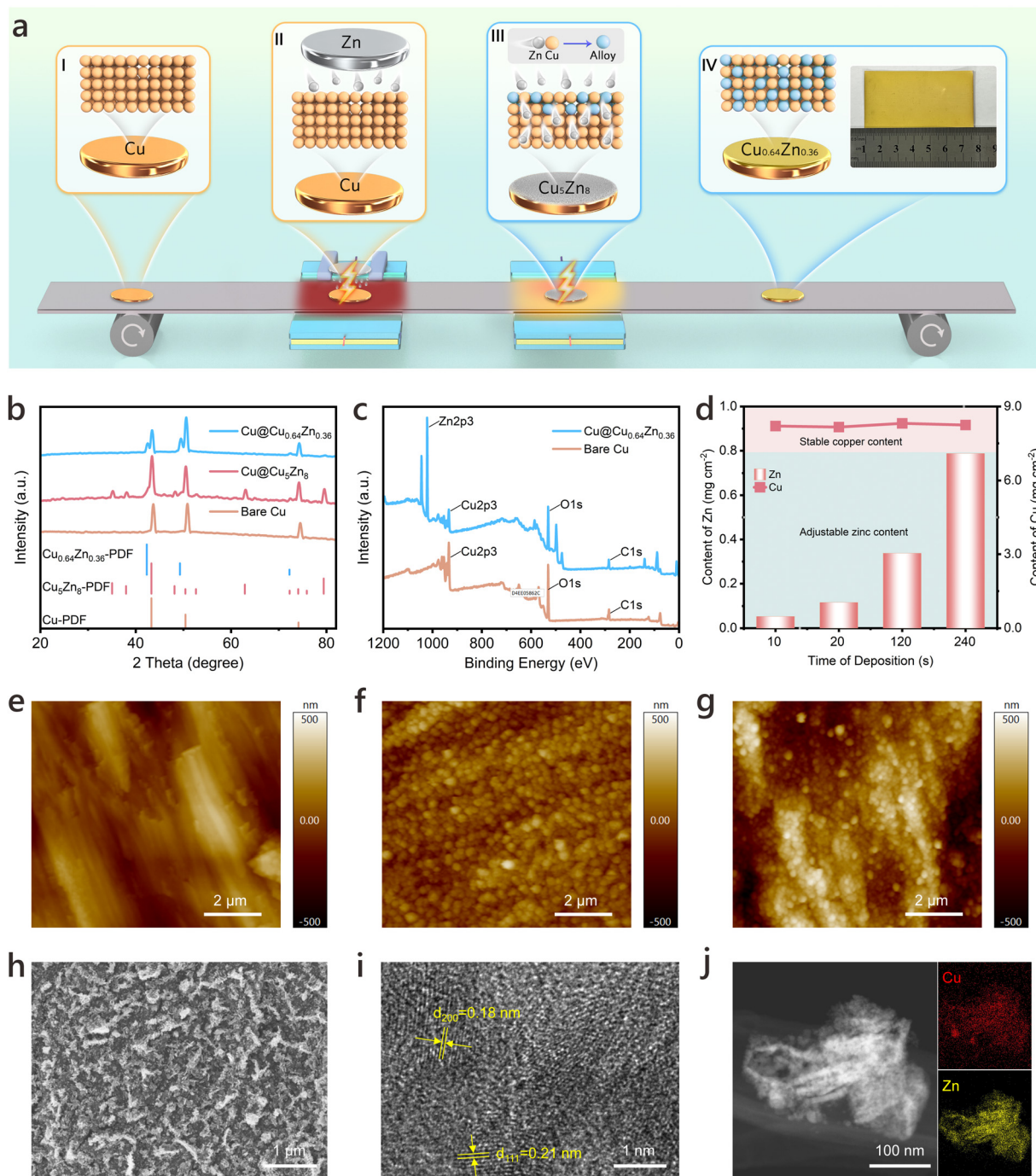
Herein, we devise and utilize the Joule heating ultrafast high-temperature (UHT) synthesis technique for the first time to rapidly, precisely, and in batch processes, prepare lithiophilic Cu–Zn alloy modification layers on the surface of Cu CCs. This strategy involves a two-step in situ alloying process applied to Cu foils (Fig. 1). Initially, the evaporated Zn forms a Cu$_5$Zn$_8$ intermediate state on the Cu surface (denoted as Cu@Cu$_5$Zn$_8$) at lower temperatures, allowing precise control of the Zn content in the alloy. The second step entails rapid and extensive alloying at elevated temperatures, resulting in a final Cu$_{0.64}$Zn$_{0.36}$ phase on the Cu surface (denoted as Cu@Cu$_{0.64}$Zn$_{0.36}$). The resultant homogeneous Cu–Zn alloy from the transient alloying reaction forms a thin lithiophilic "skin" layer, which is fundamentally distinct from traditional externally introduced alloy coatings. This approach preserves the conductivity and ductility of the thin Cu foil while significantly enhancing its wettability to metallic Li. As a result, it effectively reduces the nucleation potential for Li deposition and improves the overall performance of LMBs. Notably, the application of Cu@Cu$_{0.64}$Zn$_{0.36}$ led to improved average CE, stabilized Li morphology, and prolonged cycle life in thin-film LMBs based on LiFePO$_4$ or LiNi$_{0.9}$Co$_{0.05}$Mn$_{0.05}$O$_2$ cathodes. This study provides a feasible and promising approach to advancing the practical application of LMBs.

## 2. Results and discussion

### 2.1. Fabrication and characterization of Cu$_{0.64}$Zn$_{0.36}$ "skin" layer on Cu CCs

Fig. 1a schematically illustrates the in situ compounding of Zn onto a Cu foil using the two-step UHT method. This approach involves a series of precisely staged alloying steps that transform the surface of Cu into a lithiophilic Cu$_{0.64}$Zn$_{0.36}$ "skin" layer. In the first step, the bare Cu foil is placed on a conveyor belt (I) that moves it beneath a Zn foil layer. A moderate-power Joule heating source vaporizes the Zn, allowing the vapor to react with the Cu surface and form a Cu–Zn intermetallic compound layer (II). This initial layer, rich in high-zinc-content grains (primarily Cu$_5$Zn$_8$), is uniformly distributed on the Cu substrate, preparing it for further alloying. In the next step, a subsequent UHT step utilizing higher-power Joule heating enables deep and complete alloying of the Cu$_5$Zn$_8$ layer with the Cu substrate (III), culminating in the formation of Cu@Cu$_{0.64}$Zn$_{0.36}$. As depicted in the temperature-time relationship curve during UHT synthesis (Fig. S1, ESI†), Zn deposition occurs at approximately 750 K over tens to hundreds of seconds, while deep alloying completes in microseconds at higher temperatures. The initial step allows precise control over the alloy composition, while the subsequent deep alloying step forms a more lithiophilic alloy, characterized by a very small contact angle with molten Li (Fig. S2, ESI†), preserving the structural integrity of the substrate. Moreover, this method enables the fabrication of large-scale alloys through controlled

Fig. 1 Schematic diagram and characterization of Cu@Cu$_{0.64}$Zn$_{0.36}$ fabrication. (a) Schematic illustration of the preparation of large-scale Cu@Cu$_{0.64}$Zn$_{0.36}$ using a two-step UHT method. (b) XRD patterns of Cu, Cu@Cu$_5$Zn$_8$, and Cu@Cu$_{0.64}$Zn$_{0.36}$. (c) XPS spectra of Cu and Cu@Cu$_{0.64}$Zn$_{0.36}$. (d) ICP-OES for Cu and Zn content at different reaction times. (e)–(g) AFM images of Cu, Cu@Cu$_5$Zn$_8$, and Cu@Cu$_{0.64}$Zn$_{0.36}$. (h)–(j) FESEM, HRTEM, HAADF-STEM images and elemental mapping of Cu@Cu$_{0.64}$Zn$_{0.36}$.

heating zones (Fig. S3, ESI†). Looking forward, the compatibility with conveyor systems paves the way for large-scale mass production, offering a significant advantage over conventional techniques.

According to the Cu–Zn binary phase diagram in Fig. S4 (ESI†), the two primary stable alloy phases emerge with increasing Zn content: the β-phase (intermetallic compound) and

α-phase (solid solution),[59] corresponding to the products formed during two different reaction stages. The structures of the Cu CCs obtained through the UHT method at various stages are shown in Fig. 1b. X-ray diffraction (XRD) analysis reveals that the pristine Cu belongs to the $Fm\bar{3}m$ space group, exhibiting three characteristic peaks at 43.3°, 50.4°, and 74.1°, which correspond to the (111), (200), and (220) diffraction

2624 | Energy Environ. Sci., 2025, 18, 2622–2633

This journal is © The Royal Society of Chemistry 2025

peaks, respectively.[60] After the first stage of UHT, new peaks appear at 35.1°, 38.0°, and 48.1°, primarily related to the formation of $Cu_5Zn_8$ on the Cu surface. After the second stage, the peaks associated with $Cu_5Zn_8$ disappear, and new peaks emerge at 42.3°, 49.3°, and 72.2°, corresponding to the (111), (200), (220) planes of $Cu_{0.64}Zn_{0.36}$. The Cu foil was replaced with a Cu mesh, and its surface was treated using the two-step UHT method to enable high-resolution TEM (HRTEM) characterization. The HRTEM image of the modified Cu mesh in Fig. 1i shows the lattice spacings of 0.18 nm and 0.21 nm, corresponding to the (200) and (111) planes of $Cu_{0.64}Zn_{0.36}$, respectively. These findings are further complemented by high-angle annular dark-field scanning TEM (HAADF-STEM) images in Fig. 1j, confirming the formation of the $Cu_{0.64}Zn_{0.36}$ phase on Cu CC surface after UHT treatment. To further verify Cu–Zn alloy formation on the Cu surface, X-ray photoelectron spectroscopy (XPS) tests were conducted, as illustrated in Fig. 1c and Fig. S5 (ESI†). Comparison of Cu 2p spectra before and after Joule heating (Fig. S5a, ESI†) shows that pristine Cu exhibits both $Cu^0$ and oxide peaks, whereas $Cu@Cu_{0.64}Zn_{0.36}$ retains the same $Cu^0$ peak positions, with the formation of the alloy layer reducing the oxide signal.[50] The full XPS spectra in Fig. S5b (ESI†) and Fig. 1c display the emergence of Zn 2p peaks after UHT processes, again clearly confirming the formation of Zn-based alloys on the Cu surface.[61] An oil-based ink isolation method was employed to measure the thickness of the alloy layer, revealing that the $Cu_{0.64}Zn_{0.36}$ layer has an approximate thickness of 470 nm (Fig. S6, ESI†). The combined characterization results consistently verify that a high-purity $Cu_{0.64}Zn_{0.36}$ alloy "skin" layer is accurately prepared on the Cu surface using the two-step UHT method.

To achieve structurally and performance-superior $Cu@Cu_{0.64}Zn_{0.36}$, it is essential to optimize the synthesis conditions in stages II and III (Fig. 1a). Stage II focuses on controlling the Zn content via a specific low-temperature reaction, effectively preventing Cu deformation typically seen in conventional single-step high-temperature alloying processes. Meanwhile, the deposition time in stage II is critical, as it determines the coverage of the $Cu_5Zn_8$ alloy "skin" layer and influences the surface morphology of the final modified Cu CCs. On the other hand, stage III operates at a higher temperature to facilitate the rapid conversion of $Cu_5Zn_8$ to $Cu_{0.64}Zn_{0.36}$ without causing damage to the substrate. Given the short duration of stage III, tight control of the conditions is required to prevent the formation of undesirable products (Fig. S7, ESI†).

A series of characterizations were conducted on CCs obtained at different stages of UHT to examine changes in composition, morphology, and structure. The effect of deposition time in stage II on the Cu–Zn alloy layer's morphology was first assessed. As shown in Fig. S8 (ESI†), a deposition time of 10 s results in the formation of nanoparticles smaller than 100 nm on the Cu surface. Extending the time to 20 s produces larger particle sizes, while further extension to 120 s leads to a dense coverage of nanoparticles. A deposition time of 240 s increases Cu–Zn alloy coverage and thickness further, but results in extended transport paths for Li-ions on the surface
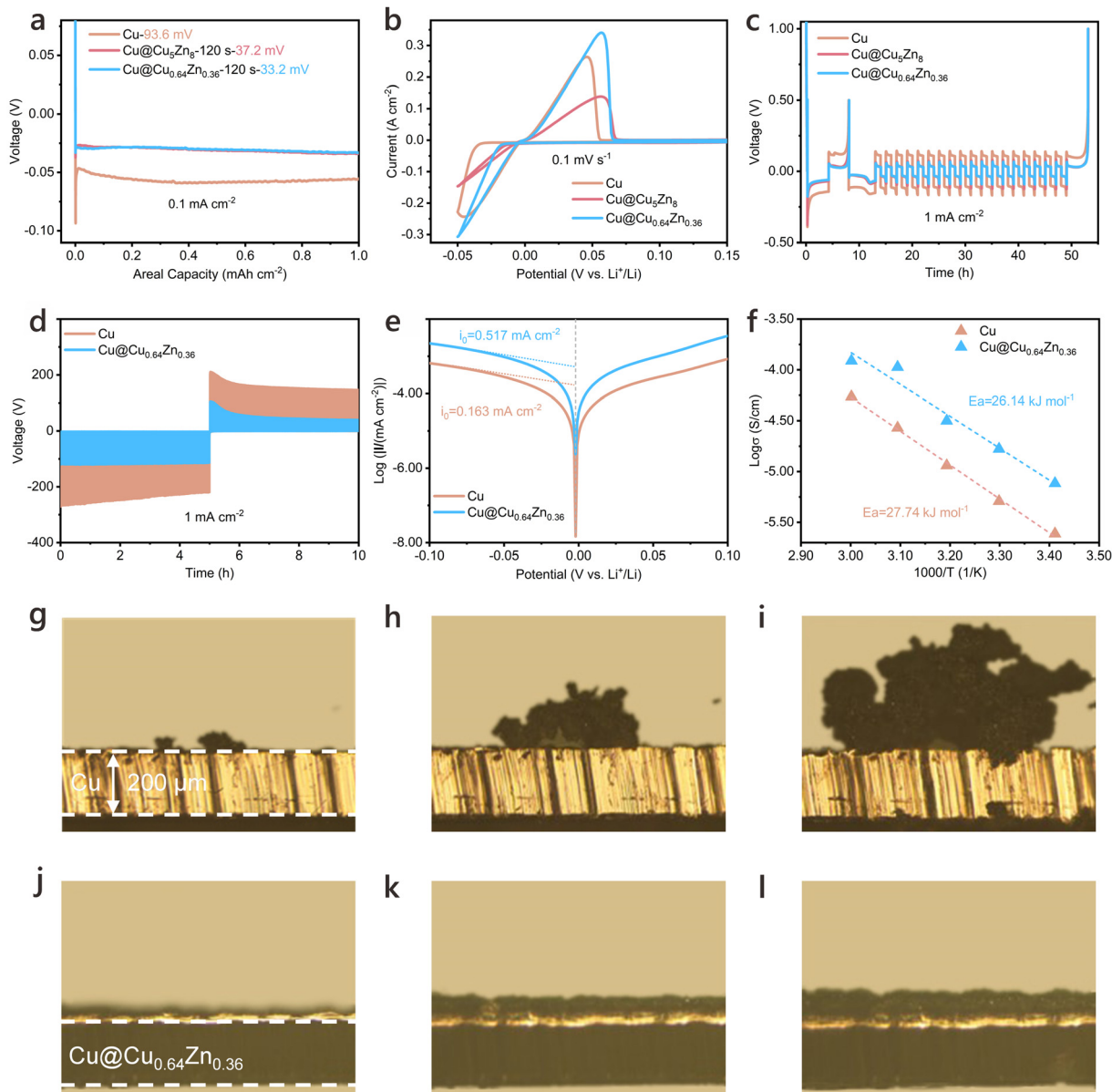
that may hinder the homogeneous Li nucleation and growth, as will be demonstrated later. Fig. 1d presents a compositional analysis of different $Cu@Cu_{0.64}Zn_{0.36}$ characterized by varying reaction time applied in stage II, using inductively coupled plasma optical emission spectroscopy (ICP-OES). The upper line graph indicates that the Cu substrate content remains stable, while the lower bar graph shows a positive correlation between deposition time and Zn content on the Cu surface, confirming increased Cu–Zn alloy layer coverage over time. Further microstructural characterization via atomic force microscopy (AFM) at different stages is shown in Fig. 1e–g. The results reveal that the pre-alloyed $Cu_5Zn_8$ significantly improves the flatness of the Cu surface compared to the rough pristine Cu surface. However, due to the rapid deep alloying reaction, $Cu_{0.64}Zn_{0.36}$ exhibits slightly increased surface roughness, as it does not fully fuse. Field emission scanning electron microscopy (FESEM) results (Fig. 1h and Fig. S9, ESI†) display that after the two-step UHT treatment, $Cu@Cu_{0.64}Zn_{0.36}$ features a continuous nanoparticle structure, consistent with the AFM findings. Energy dispersive X-ray spectroscopy (EDS) mapping further manifests a uniform distribution of Cu and Zn across the $Cu@Cu_{0.64}Zn_{0.36}$ surface, with a stronger Cu signal compared to Zn (Fig. S10, ESI†).

Electrochemical tests were performed to compare the effects of Cu CCs with varying coverages of the Cu–Zn alloying layer on Li deposition behaviour. The results indicate that the nucleation overpotentials for Li on alloyed Cu surfaces are significantly reduced, and the Li deposition plateau potentials are greatly improved compared to pristine Cu (Fig. S11, ESI†). Notably, these results collectively confirm that the sample alloyed for 120 s exhibits optimal structural and performance characteristics. This Cu–Zn alloy formation enhances the lithiophilicity of the Cu surface, reduces the local aggregation of Li-ions, and promotes a uniform Li distribution, resulting in highly reversible and stable Li plating and stripping behaviour. However, when the alloying time was extended to 240 s, the polarization during Li deposition increased. This is attributed to excessive and inhomogeneous island-like alloy formation, which prolongs the local Li-ion diffusion path and reduces mass transport efficiency. Unless otherwise stated, $Cu@Cu_{0.64}Zn_{0.36}$ was prepared with preliminary alloying for 120 s and deep alloying for 30 ms.

## 2.2. The enhanced kinetics of lithium deposition on $Cu@Cu_{0.64}Zn_{0.36}$

To evaluate the modulatory effect of the alloy-modified Cu CCs on Li metal deposition behaviour, Li||Cu half cells were assembled for a series of electrochemical studies. The overpotentials for Li deposition on different Cu CCs were first investigated. As shown in Fig. 2a, the Li nucleation overpotential on $Cu@Cu_{0.64}Zn_{0.36}$ is reduced to 33.2 mV at 0.1 mA $cm^{-2}$, compared to 37.2 mV on $Cu@Cu_5Zn_8$ and 93.6 mV on pristine Cu. Apart from the low nucleation overpotential, $Cu@Cu_{0.64}Zn_{0.36}$ also exhibits a significantly lower growth overpotential, evidenced by the low potential hysteresis during deposition. The differences in Li deposition among the three Cu CCs were also evaluated using cyclic

Fig. 2 Kinetics of lithiophilic mechanisms of modified Cu CCs. (a) Potential–capacity profiles of Cu, Cu@Cu$_5$Zn$_8$, and Cu@Cu$_{0.64}$Zn$_{0.36}$ at 0.1 mA cm$^{-2}$. (b) CV curves of Cu, Cu@Cu$_5$Zn$_8$, and Cu@Cu$_{0.64}$Zn$_{0.36}$ in LillCu cells. (c) Time–voltage profiles of LillCu cells with Cu, Cu@Cu$_5$Zn$_8$, and Cu@Cu$_{0.64}$Zn$_{0.36}$ by the Aurbach method. (d)–(f) GITT profiles (d), Tafel plots (e), and the activation energies of $R_{SEI}$ (f) of Cu and Cu@Cu$_{0.64}$Zn$_{0.36}$ illustrating the kinetics of Li deposition. (g)–(l) In situ optical microscopy observations of the Li plating on Cu (g)–(i) and Cu@Cu$_{0.64}$Zn$_{0.36}$ (j)–(l) at 5 mA cm$^{-2}$ for 5 min, 20 min, and 40 min.

voltammetry (CV), where Cu@Cu$_{0.64}$Zn$_{0.36}$ has a markedly lower Li deposition overpotential compared to the other two CCs, characterized by a more pronounced and steeper current peak at the same deposition potential (Fig. 2b). This substantial decrease in overpotential highlights the superior Li nucleation and growth behavior on Cu@Cu$_{0.64}$Zn$_{0.36}$, which indicates a more efficient Li-ion transport and deposition kinetic. Additionally, CE measurements based on the method by Aurbach further validate the benefits of Cu@Cu$_{0.64}$Zn$_{0.36}$ (Fig. 2c). Among all tested samples, Cu@Cu$_{0.64}$Zn$_{0.36}$ exhibits the least additional Li consumption and consistently maintains the highest CE over prolonged cycling. Moreover, it significantly reduces potential hysteresis compared

to both pristine Cu and Cu@Cu$_5$Zn$_8$. This optimized performance underscores the enhanced cycling stability and reduced polarization of Li deposition/dissolution on Cu@Cu$_{0.64}$Zn$_{0.36}$.

The galvanostatic intermittent titration technique (GITT) was employed to further investigate and compare the kinetic differences in Li deposition/dissolution on varying Cu CCs,[62] as shown in Fig. 2d. Initially, Li was deposited on the CCs at 0.5 mA cm$^{-2}$ for 8 h to form a metallic Li layer approximately 20 μm thick. Subsequently, Li was deposited intermittently 120 times at 1 mA cm$^{-2}$ for 30 s per cycle, with a 2-min rest period between cycles under intermittent conditions. The stripping process followed a similar protocol. The results indicate

2626 | Energy Environ. Sci., 2025, 18, 2622–2633

This journal is © The Royal Society of Chemistry 2025

that the optimized $Cu@Cu_{0.64}Zn_{0.36}$ exhibits lower Li nucleation barriers and polarization, reflecting a homogeneous Li nucleation mechanism. This improvement is attributed to the $Cu_{0.64}Zn_{0.36}$ "skin" layer, which enhances the affinity between Li and the CC. This reduction in the nucleation barrier for $Li^+$ aids in rapid charge transfer, promoting uniform Li metal deposition on the $Cu@Cu_{0.64}Zn_{0.36}$ surface.

The improvement in Li deposition kinetics is also supported by the exchange current density ($i^0$) calculated from the fitted Tafel plots.[63] As shown in Fig. 2e, the $i^0$ for $Cu@Cu_{0.64}Zn_{0.36}$ is 0.517 mA cm$^{-2}$, significantly higher than that of pristine Cu (0.163 mA cm$^{-2}$). These results indicate that the nucleation kinetics of $Li^+$ on $Cu@Cu_{0.64}Zn_{0.36}$ are considerably enhanced, likely due to the stronger bonding interactions between Li and $Cu_{0.64}Zn_{0.36}$. This enhancement in nucleation and charge transfer properties underscores the effectiveness of the $Cu_{0.64}Zn_{0.36}$ layer in facilitating uniform Li metal deposition on CCs.

Electrochemical impedance spectroscopy (EIS) was conducted on the Li||Cu and Li||Cu@Cu$_{0.64}$Zn$_{0.36}$ cells after 5 cycles at varying temperatures, as illustrated in Fig. 2f and Fig. S12 (ESI†). The results show that the SEI resistances of the Li||Cu@Cu$_{0.64}$Zn$_{0.36}$ cells are consistently lower than those of the Li||Cu cells. By linearly fitting $\log(1/R_{SEI})$ against $1/T$,[64] the apparent activation energies for Li-ion transport through SEIs are determined as 27.74 kJ mol$^{-1}$ for Li||Cu and 26.14 kJ mol$^{-1}$ for Li||Cu@Cu$_{0.64}$Zn$_{0.36}$. This suggests that alongside modulating the Li plating and stripping behaviour, the $Cu_{0.64}Zn_{0.36}$ "skin" layer promotes the formation of the superior interface that facilitates Li-ion transport. XPS analysis further corroborates this, showing that the SEI layer on $Cu@Cu_{0.64}Zn_{0.36}$ displays markedly enhanced C–F (ca. 688.2 eV) and LiF (ca. 685.3 eV) peaks from the surface to the interior after cycling. The total average atomic F content increased from 4.93% to 18.93%, while the content of C and O species (such as C–O, C=O, ROCO$_2$Li,) are lower than those on pristine Cu (Fig. S13, ESI†).[63] The increase in LiF content indicates that the strength of SEI is reinforced. Moreover, the corresponding modulus mapping reveals that the SEI on the $Cu@Cu_{0.64}Zn_{0.36}$ has a higher Young's modulus (Fig. S14, ESI†), indicating a more robust SEI structure. These findings confirm that the $Cu_{0.64}Zn_{0.36}$ "skin" layer on Cu CCs positively influences SEI composition and mechanical properties, enhancing Li-ion transport and SEI stability during cycling.

*In situ* metallurgical microscopy was used to observe Li deposition on different CCs to evaluate their influence on dendrite growth. Fig. 2g–l manifests the morphologies of plated Li on pristine Cu and $Cu@Cu_{0.64}Zn_{0.36}$ after 5, 20, and 40 min of deposition at 5 mA cm$^{-2}$. On pristine Cu, inhomogeneous Li aggregates occur in the initial 5 min, with pronounced dendritic growth emerging as deposition progresses. In contrast, $Cu@Cu_{0.64}Zn_{0.36}$ exhibits uniform and flat Li deposition, gradually forming a smooth Li layer. This uniform deposition is attributed to the favorable lithiophilicity of the $Cu_{0.64}Zn_{0.36}$ layer, which lowers the Li nucleation barrier and minimizes dendrite formation. FESEM provides further insights into Li deposition morphology at 4 mA h cm$^{-2}$ and 10 mA h cm$^{-2}$,
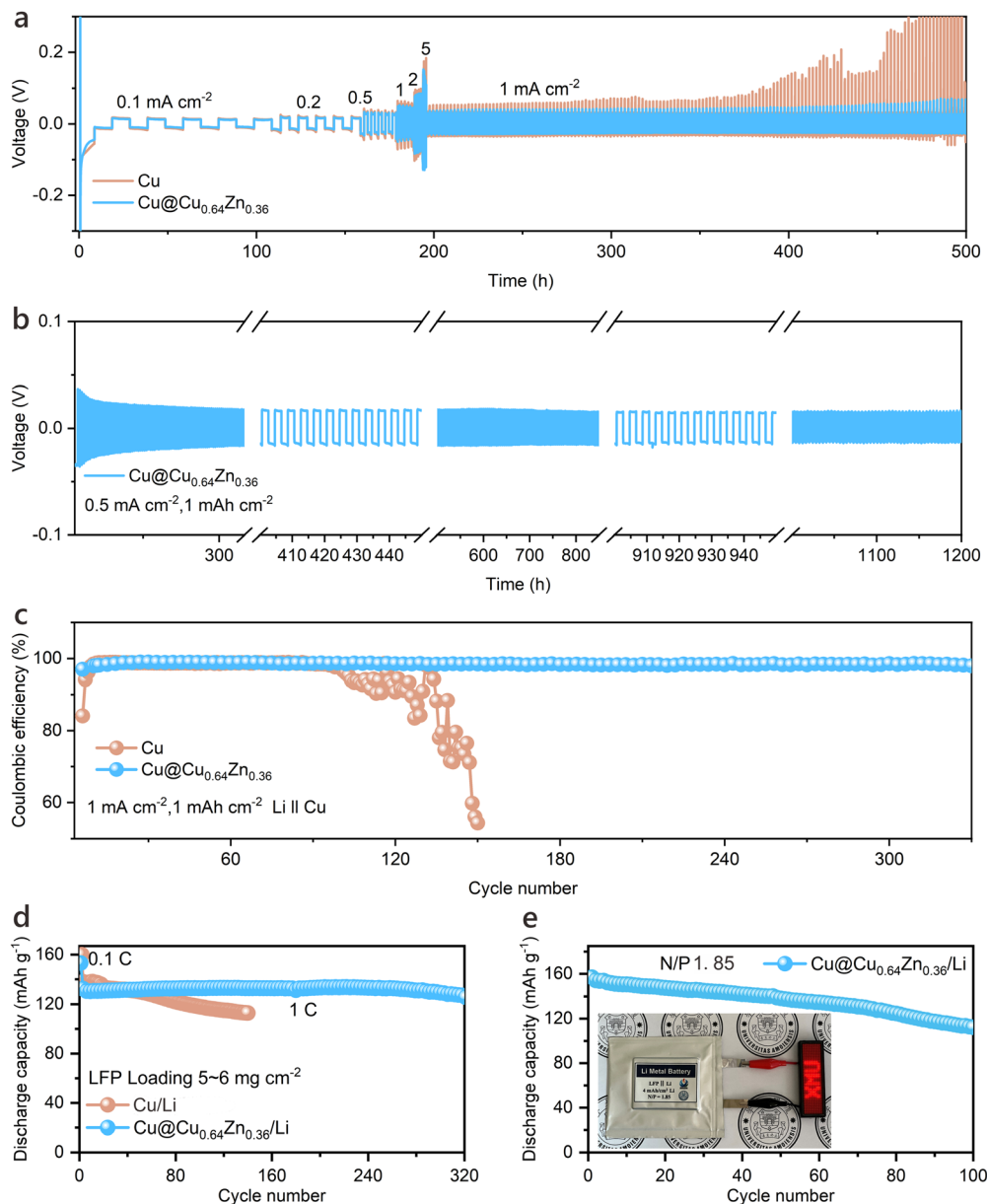
captured both on the surface and in cross-sectional views (Fig. S15 and S16, ESI†). On $Cu@Cu_{0.64}Zn_{0.36}$, Li forms larger, denser particles without elongated dendritic structures, maintaining a smooth surface morphology even after 50 cycles (Fig. S17, ESI†). Additionally, after the deposition and dissolution of 10 mA h cm$^{-2}$ of Li, XRD analysis of the disassembled $Cu@Cu_{0.64}Zn_{0.36}$ shows that its surface structure remains stable, with no detectable structural changes except for the appearance of a Li peak at 36.2° (Fig. S18, ESI†). Moreover, the structural stability of $Cu@Cu_{0.64}Zn_{0.36}$ during electrochemical cycling was verified by XRD and ICP analyses performed after 50 cycles in Li||Cu cells under 1 mA cm$^{-2}$, 1 mA h cm$^{-2}$ (Fig. S19, ESI†). The XRD patterns show identical peak positions and relative intensities compared to the pristine sample, while ICP results confirm that the Cu and Zn contents are nearly unchanged after cycling, collectively demonstrating the excellent structural stability of $Cu@Cu_{0.64}Zn_{0.36}$. The above results consistently demonstrate the superior properties of the novel $Cu@Cu_{0.64}Zn_{0.36}$ developed using UHT method, underscoring its effectiveness in promoting uniform Li deposition and maintaining structural stability during cycling.

### 2.3. $Cu@Cu_{0.64}Zn_{0.36}$ enables highly-reversible LMBs

The practical application potential of ultrathin Li prepared on modified Cu CCs in LMBs was assessed through electrochemical tests in both ether-based and ester-based electrolytes, as shown in Fig. 3 and 4. Tests included Li||Li and Li||Cu cells with 4 mA h cm$^{-2}$ of Li deposited on the CCs using an electrolyte of 1 M LiTFSI/DOL-DME (1 : 1, v/v) with 2 wt% LiNO$_3$. Results reveal that the $Cu@Cu_{0.64}Zn_{0.36}$-based Li anodes exhibit consistently low voltage hysteresis at various current densities, maintaining a polarization voltage of approximately 14.6 mV for extended periods, up to 1200 hours in Li||Li symmetric cells (Fig. 3a and b). Further testing in Li||Cu cells highlights the high efficiency of $Cu@Cu_{0.64}Zn_{0.36}$-based Li anode, which achieves an initial efficiency superior to other tested CCs and maintains a high CE of 98.5% after 330 cycles with plating/stripping at 1 mA cm$^{-2}$ and 1 mA h cm$^{-2}$ (Fig. 3c and Fig. S20, ESI†). Under similar conditions, pristine Cu stabilizes for only around 95 cycles. Additionally, $Cu@Cu_{0.64}Zn_{0.36}$ shows stable, low Li deposition overpotential across a current gradient ranging from 0.1 to 5 mA cm$^{-2}$, as indicated in Fig. S21 (ESI†).

In addition to half-cell testing, a full-cell configuration was also evaluated. A finite amount of Li metal (4 mA h cm$^{-2}$) was pre-deposited on the CCs and paired with a LiFePO$_4$ (LFP) cathode to form a Li||LFP full battery (Fig. S22, ESI†). As depicted in Fig. 3d, the battery's discharge capacity remains relatively stable throughout cycling, attributed to the excellent affinity of $Cu@Cu_{0.64}Zn_{0.36}$ for Li metal. This configuration achieves a high capacity retention rate of 95% after 320 cycles at 1C, significantly outperforming the continuously decreasing specific capacity observed with pristine Cu. To further assess the performance of current collectors under extreme conditions, batteries with anode-free configuration were conducted. $Cu@Cu_{0.64}Zn_{0.36}$ exhibits higher reversible capacity and superior capacity retention (60.3%) compared to bare Cu (14.2%),

This journal is © The Royal Society of Chemistry 2025

*Energy Environ. Sci.*, 2025, **18**, 2622–2633 | **2627**

**Fig. 3** Electrochemical performance of half-cells and full-batteries with ether-based electrolytes. (a) Rate capabilities of thin film Li||Li symmetric cells with 4 mA h cm$^{-2}$ Li pre-deposited on Cu CCs at varying current densities. (b) Galvanostatic cycling of Li||Li symmetric cells with 4 mA h cm$^{-2}$ Li pre-deposited on Cu@Cu$_{0.64}$Zn$_{0.36}$ at 0.5 mA cm$^{-2}$ and 1 mA h cm$^{-2}$. (c) Comparison of CEs for various Li||Cu cells at 1 mA cm$^{-2}$ and 1 mA h cm$^{-2}$. (d) Long-term cycling performance of Li||LFP full batteries at 1C with Li anodes formed by pre-depositing 4 mA h cm$^{-2}$ Li on Cu CCs. (e) Cycling performance of Li||LFP pouch batteries with the Cu@Cu$_{0.64}$Zn$_{0.36}$-based Li thin-film anode at 0.1C. The inset shows an optical photograph of the battery powering a LED device.
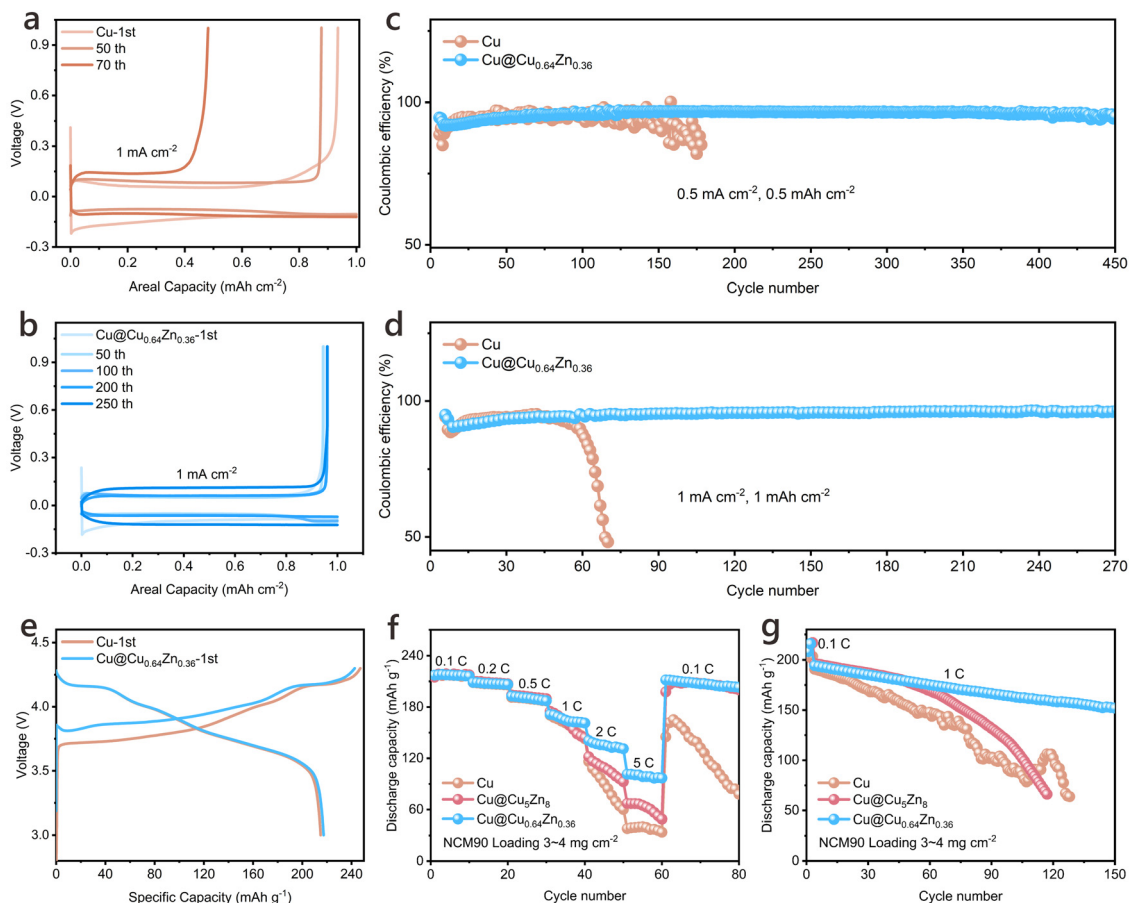
highlighting the robustness of our design even under very harsh testing scenario (Fig. S23, ESI†). Moreover, a laboratory-scale Joule heating unit was developed, capable of preparing tens of square centimetres of material at a time, with the potential for further production line expansion. This approach enables the preparation of large-area Cu@Cu$_{0.64}$Zn$_{0.36}$ paired with high-loading LFP cathode, achieving a pouch cell with a negative/positive (N/P) capacity ratio of 1.85. This configuration demonstrates stable cycling performance and successfully powers a series of XMU light-emitting diode (LED) lights

(Fig. 3e), highlighting the potential of Cu@Cu$_{0.64}$Zn$_{0.36}$ to enhance battery lifespan and efficiency in practical applications.

To further probe the potential of Cu@Cu$_{0.64}$Zn$_{0.36}$ in LMBs involving carbonate-based electrolyte, Li||Cu half cells were constructed with an electrolyte of 1 M LiPF6/EC-DMC-DEC containing 10% FEC and 2% VC. As shown in Fig. 4a–d, the cells using Cu@Cu$_{0.64}$Zn$_{0.36}$ demonstrate stable cycling in this high side-reaction activity environment. These cells maintain stable cycling for about 270 cycles at 1 mA cm$^{-2}$ and 1 mA h cm$^{-2}$, achieving a CE of over 96%. This is significantly superior to those

**2628** | *Energy Environ. Sci.*, 2025, **18**, 2622–2633

This journal is © The Royal Society of Chemistry 2025

**Fig. 4** Electrochemical performance of half-cells and full-batteries with carbonate-based electrolytes. (a) and (b) Voltage−capacity profiles of LillCu cells using Cu (a) and Cu@Cu$_{0.64}$Zn$_{0.36}$ (b) after different cycle numbers. (c) and (d) Comparison of CEs for various LillCu cells at 0.5 mA cm$^{-2}$ (c) and 1 mA cm$^{-2}$ (d). (e) The initial galvanostatic charge−discharge curves of different LillNCM90 full batteries at 0.1C with Li anodes formed by pre-depositing 4 mA h cm$^{-2}$ Li on different Cu CCs. Rate capacity (f) and cycling performance (g) of various LillNCM90 batteries with the NCM90 mass loading of 3.0−4.0 mg cm$^{-2}$ and Li anodes formed by pre-depositing 4 mA h cm$^{-2}$ Li on different Cu CCs.

cells using pristine Cu, which fall below 50% CE after 69 cycles. Even at a high current density (5 mA cm$^{-2}$), LillCu cells equipped with Cu@Cu$_{0.64}$Zn$_{0.36}$ maintain stable cycling for about 240 cycles (Fig. S24 and S25, ESI†). EIS was used to evaluate impedance in LillCu cells after various cycles, consistently showing lower $R_{SEI}$ and $R_{ct}$ in cells with Cu@Cu$_{0.64}$Zn$_{0.36}$ (Fig. S26, ESI†). This highlights its ability to stabilize the anode/electrolyte interface and reduce active Li loss, thus improving cycling stability. (Fig. S27, ESI†) To further assess the compatibility with cathode materials in carbonate-based electrolyte, a high-nickel-content LiNi$_{0.9}$-Co$_{0.05}$Mn$_{0.05}$O$_2$ (NCM90) cathode was matched with Cu@Cu$_{0.64}$Zn$_{0.36}$-based Li anode (Fig. 4e). The resultant full battery exhibits outstanding rate performance, delivering specific capacities of 217, 209, 193, 171, 141, 101, and 212 mA h g$^{-1}$ at 0.1, 0.2, 0.5, 1, 2, 5C, and back to 0.1C, respectively (Fig. 4f). Moreover, these full batteries show excellent cycling stability over 150 cycles at a rate of 1C, in the voltage range of 3 to 4.3 V (Fig. 4g and Fig. S28, ESI†). All these findings underscore the Cu@Cu$_{0.64}$Zn$_{0.36}$'s suitability for practical applications, given its low polarization, prolonged cycle stability, and high
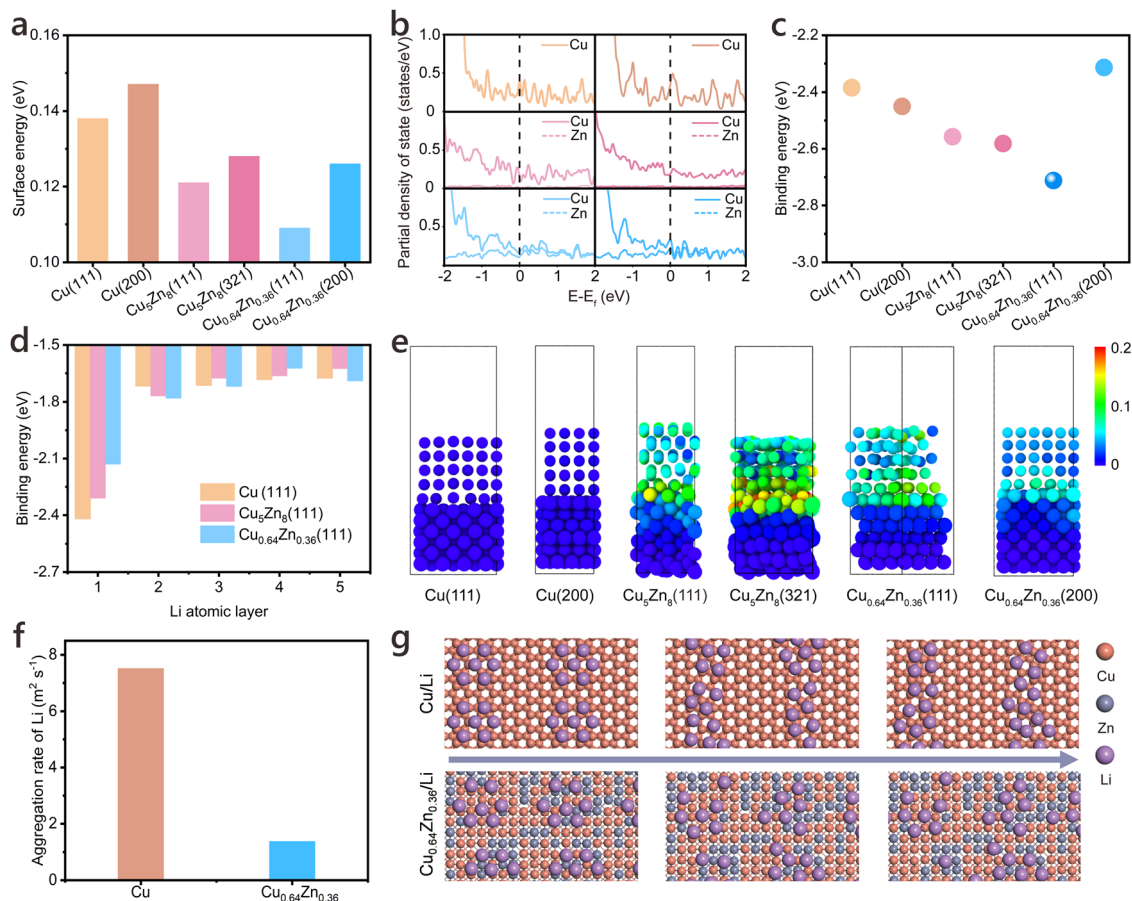
efficiency across varying current densities, highlighting its potential as a reliable CC for advanced LMB systems.

## 2.4. Theoretical calculations of the lithiophilic mechanism of Cu@Cu$_{0.64}$Zn$_{0.36}$

To elucidate the role of Cu–Zn alloys in regulating Li deposition behaviour, we performed theoretical simulations of Li inter-action with various Cu–Zn CCs, as illustrated in Fig. 5. Initially, the structural stability of different CCs was evaluated by calcu-lating their surface energies (Fig. 5a). The surface energies of Cu$_{0.64}$Zn$_{0.36}$ (111) and (200) planes were calculated to be 0.109 eV and 0.126 eV, respectively, significantly lower than those of the corresponding Cu$_5$Zn$_8$ and pure Cu planes. This indi-cates that the most probable surfaces of Cu$_{0.64}$Zn$_{0.36}$ exhibit enhanced stability and are less prone to collapse during cycling. Analysis of the partial density of states (PDOS) reveals that, unlike pure Cu, which exhibits excellent conductivity, Zn in Cu$_5$Zn$_8$ contributes negligibly to electron transport (Fig. 5b). Conversely, Zn in Cu$_{0.64}$Zn$_{0.36}$ shows comparable occupancy at the Fermi level with Cu, suggesting a positive contribution of

This journal is © The Royal Society of Chemistry 2025

*Energy Environ. Sci.*, 2025, **18**, 2622–2633 | **2629**

Fig. 5 Theoretical calculations the lithiophilic mechanism in Cu–Zn alloys. (a) Surface energies of primary crystal planes of Cu, $Cu_5Zn_8$, and $Cu_{0.64}Zn_{0.36}$. (b) Partial density of states distribution of Cu, $Cu_5Zn_8$, and $Cu_{0.64}Zn_{0.36}$. (c) Binding energy of single-layer Li atom on Cu, $Cu_5Zn_8$, $Cu_{0.64}Zn_{0.36}$. (d) Binding energy of multilayered Li on the (111) crystal planes of Cu, $Cu_5Zn_8$, $Cu_{0.64}Zn_{0.36}$. (e) Deposition arrangement of 5 Li layers on Cu and $Cu_{0.64}Zn_{0.36}$. (f) and (g) Aggregation rate (f) and distribution pattern (g) of Li on Cu and $Cu_{0.64}Zn_{0.36}$.

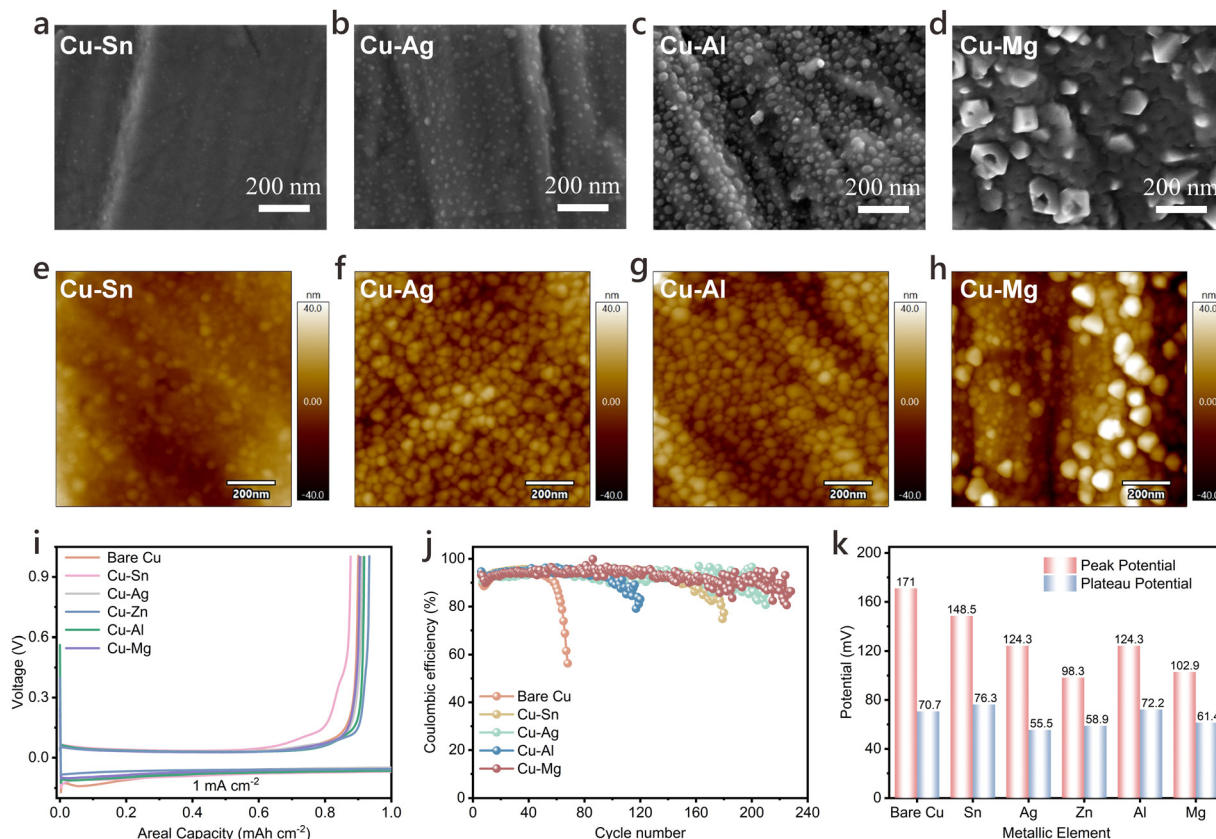Zn to electron transport and thus favourable electrochemical performance.

Fig. 5c displays the binding energy of a single Li atom on different crystal surfaces. The (111) plane of $Cu_{0.64}Zn_{0.36}$ exhibits the highest Li binding energy, consistent with previous reports.[65,66] Subsequently, we investigated multilayer Li deposition, focusing on the (111) planes of the three substrates (Fig. 5d). Unlike the single-atom case, during multilayer deposition, the Li-CCs binding energy is influenced by the lattice mismatch between the Li crystal and the substrate. For $Cu_{0.64}Zn_{0.36}$(111), the binding energy of the initial Li layer is relatively weak, contrasting with the single-atom scenario. This suggests a poor lattice match between $Cu_{0.64}Zn_{0.36}$(111) and Li, leading to significant lattice distortion. In subsequent layers, the decrease in Li binding energy is significantly greater for $Cu_{0.64}Zn_{0.36}$(111) and $Cu_5Zn_8$(111) than for Cu(111) (Fig. 5e), indicating that the extent and impact of the lattice distortion are more pronounced in the former, effectively mitigating Li dendrite formation. Molecular dynamics (MD) simulations were employed to dynamically study the aggregation behaviour of Li on Cu and $Cu_{0.64}Zn_{0.36}$ surfaces. The aggregation rate serves as a crucial indicator of Li deposition uniformity, where

a lower value suggests more uniform Li distribution and reduced dendrite formation. This parameter reflects the surface lithiophilicity and Li diffusion behavior, directly correlating with the electrode's ability to achieve stable and reversible Li plating/stripping. Fig. 5f and g illustrate the dispersion of Li atoms and their temporal evolution on Cu(111) and $Cu_{0.64}Zn_{0.36}$(111) substrates. The aggregation rate of Li atoms is markedly higher on the pure Cu surface, leading to rapid Li accumulation, whereas Li atoms remain largely dispersed on the $Cu_{0.64}Zn_{0.36}$ surface. This characteristic promotes uniform Li deposition on $Cu_{0.64}Zn_{0.36}$, effectively suppressing dendrite growth.

## 2.5. Universality of UHT method extensions in alloy modification for CCs

The UHT technique, a highly efficient and rapid heating method, has been extensively applied in groundbreaking research and is introduced here for the first time to modify CCs in LMBs. The Cu–Zn alloy serves as a lithiophilic modification, effectively lowering the nucleation barrier of Li and transforming both the intrinsic properties of the CCs and the distribution of surface electric and ionic fields. This

2630 | Energy Environ. Sci., 2025, 18, 2622–2633

This journal is © The Royal Society of Chemistry 2025

Fig. 6 Universality and expansion of the UHT method for alloy skin preparation on Cu CCs. (a)–(d) FESEM images of Cu–Sn, Cu–Ag, Cu–Al, and Cu–Mg alloy layers on Cu CCs. (e)–(h) AFM images of Cu–Sn, Cu–Ag, Cu–Al, and Cu–Mg alloy layers on Cu CCs. (i) and (j) Voltage–capacity profiles (i) and cycling performance (j) of LillCu cells with various alloy-modified Cu CCs. (k) Overpotential diagram for LillCu cells with various alloy-modified Cu CCs.

modification approach can extend to various metals. Based on existing research, Sn, Ag, Al, and Mg, each exhibiting unique lithiophilic characteristics, were selected for further investigation. Given their different melting and boiling points and alloying potential with Cu, a slow vapor deposition near each metal's melting point was employed. Fig. 6a–d display the morphologies of these metals deposited on commercial Cu CCs, with their contents verified by ICP-OES (Fig. S29, ESI†).

For instance, metallic Sn, with a melting point of 505.04 K, exhibits extensive vapor diffusion at lower temperatures, leading to nanoscale particle deposition on the Cu CC. In contrast, higher-melting-point metals such as Ag and Al form nearly spherical particles, while Mg aggregates into irregular crystalline structures. AFM images in Fig. 6e–h shows morphologies corresponding to Fig. 6a–d, revealing that fine, uniformly deposited Ag and Al particles smooth the natural roughness of Cu. A comparative analysis of the different alloys prepared *via* UHT for Li deposition in LillCu half-cells is shown in Fig. 6i. Among these, the Cu–Ag alloy demonstrates the lowest overpotential for Li plating, and the Cu–Mg alloy achieves the longest cycle life, while the optimized Cu–Zn alloy provides the lowest nucleation overpotential (Fig. 6j and k). Collectively, modifying CCs with uniformly fine particles enhances performance over pristine Cu, offering valuable insights for further CC modifications in LMBs. Our self-optimized equipment has

successfully achieved small-batch production of modified Cu current collectors with large-area uniformity, demonstrating significant potential for future scale-up manufacturing.

## 3. Conclusions

In summary, an improved UHT method has been developed to fabricate a lithiophilic Cu–Zn alloy "skin" layer on Cu, allowing for precise control over alloy composition to optimize the performance of Cu CCs in thin-film LMBs. Experimental results, corroborated by theoretical calculations, confirm that the lithiophilic layer comprises highly dispersed $Cu_{0.64}Zn_{0.36}$, which improves $Li^+$ diffusion kinetics and lowers the nucleation barrier. This regulated surface facilitates high-quality Li deposition on the CCs, yielding exceptional electrochemical performance. The $Cu@Cu_{0.64}Zn_{0.36}$ CCs enable reversible Li plating-stripping with enhanced CE in half cells using ether-based electrolyte. When matched with LFP or NCM90 cathodes in full batteries, they exhibit superior cycling stability and high capacity retention. This method is effective not only for producing superior Cu–Zn alloys, but also for fabricating various alloy "skin" layers with controlled composition and structure to improve lithiophilicity. Additionally, a laboratory-scale Joule heating unit has been constructed, capable of preparing tens

of square centimetres of material at a time. This approach significantly reduces both energy consumption and processing time, setting a foundation for the large-scale production of high-performance modified CCs for LMBs.

## Author contributions

Y. G. and L. Z. designed and supervised this work. H. W., Y. M., and P. X. carried out the synthesis and the electrochemical experiments. H. W., Y. M., Y. D., performed *in situ* optical microscopy, XRD, ICP-OES, Raman, XPS, FESEM, AFM and TEM characterizations. J. H. carried out DFT calculations. H. W., and P. X. wrote the manuscript. L. Z., Y. G., J. H., J. L., B. M. appraised and revised the paper. H. Y. participated in the analysis of experimental data and the discussion of results, as well as the preparation of the manuscript.

## Data availability

The data that support the findings of this study are available on request from the corresponding authors, experiments: Dr Yu Gu, ygu@xmu.edu.cn and Prof. Li Zhang, zhangli81@xmu.e-du.cn. Calculations: Prof. Jiajia Han, jiajiahan@xmu.edu.cn, upon reasonable request.

## Conflicts of interest

The authors declare no conflict of interest.

## Acknowledgements

## References

1 J. Liu, Z. Bao, Y. Cui, E. J. Dufek, J. B. Goodenough, P. Khalifah, Q. Li, B. Y. Liaw, P. Liu, A. Manthiram, Y. S. Meng, V. R. Subramanian, M. F. Toney, V. V. Viswanathan, M. S. Whittingham, J. Xiao, W. Xu, J. Yang, X.-Q. Yang and J.-G. Zhang, *Nat. Energy*, 2019, **4**, 180–186.

2 X. R. Chen, B. C. Zhao, C. Yan and Q. Zhang, *Adv. Mater.*, 2021, **33**, e2004128.

3 J. L. Yang, M. H. Li, Z. J. Sun, X. Lian, Y. A. Wang, Y. X. Niu, C. L. Jiang, Y. N. Luo, Y. Liu, Z. L. Tian, Y. Long, K. Zhang, P. C. Yu, J. Zhang, Z. H. Wang, G. Wu, M. Gu and W. Chen, *Energy Environ. Sci.*, 2023, **16**, 3837–3846.

4 S. Zhai, N. Wang, X. Tan, K. Jiang, Z. Quan, Y. Li and Z. Li, *Adv. Funct. Mater.*, 2021, **31**, 2008894.

5 S. Li, J. Lin, Y. Ding, P. Xu, X. Guo, W. Xiong, D. Y. Wu, Q. Dong, J. Chen and L. Zhang, *ACS Nano*, 2021, **15**, 13803.

6 Y. Gu, W. W. Wang, Y. J. Li, Q. H. Wu, S. Tang, J. W. Yan, M. S. Zheng, D. Y. Wu, C. H. Fan, W. Q. Hu, Z. B. Chen, Y. Fang, Q. H. Zhang, Q. F. Dong and B. W. Mao, *Nat. Commun.*, 2018, **9**, 1339.

7 H. Pan, L. Wang, Y. Shi, C. Sheng, S. Yang, P. He and H. Zhou, *Nat. Commun.*, 2024, **15**, 2263.

8 Y. Gu, E. M. You, J. D. Lin, J. H. Wang, S. H. Luo, R. Y. Zhou, C. J. Zhang, J. L. Yao, H. Y. Li, G. Li, W. W. Wang, Y. Qiao, J. W. Yan, D. Y. Wu, G. K. Liu, L. Zhang, J. F. Li, R. Xu, Z. Q. Tian, Y. Cui and B. W. Mao, *Nat. Commun.*, 2023, **14**, 3536.

9 H. S. Wang, Z. Yu, X. Kong, S. C. Kim, D. T. Boyle, J. Qin, Z. N. Bao and Y. Cui, *Joule*, 2022, **6**, 588.

10 M. Y. Gu, A. M. Rao, J. Zhou and B. A. Lu, *Energy Environ. Sci.*, 2023, **16**, 1166–1175.

11 X. Zhang, P. Xu, J. Duan, X. Lin, J. Sun, W. Shi, H. Xu, W. Dou, Q. Zheng, R. Yuan, J. Wang, Y. Zhang, S. Yu, Z. Chen, M. Zheng, J.-F. Gohy, Q. Dong and A. Vlad, *Nat. Commun.*, 2024, **15**, 536.

12 P. Zhai, T. Wang, H. Jiang, J. Wan, Y. Wei, L. Wang, W. Liu, Q. Chen, W. Yang, Y. Cui and Y. Gong, *Adv. Mater.*, 2021, **33**, e2006247.

13 X. B. Cheng, R. Zhang, C. Z. Zhao and Q. Zhang, *Chem. Rev.*, 2017, **117**, 10403.

14 R. Fang, Y. X. Li, W. W. Wang, Y. Gu and B. W. Mao, *Phys. Chem. Chem. Phys.*, 2024, **26**, 23544.

15 C. Yan, Y. X. Yao, X. Chen, X. B. Cheng, X. Q. Zhang, J. Q. Huang and Q. Zhang, *Angew. Chem., Int. Ed.*, 2018, **57**, 14055.

16 S. Pal, X. Lin, P. Apostol, C. Ungureanu, D. Tie, V. R. Bakuru, D. Rambabu, N. Campagnol, A. Kachmar, C. Poleunis, G. Barozzino-Consiglio, M. Buga and A. Vlad, *ACS Energy Lett.*, 2024, **9**, 4399–4407.

17 Q. Peng, Z. Liu, L. Jiang and Q. Wang, *Adv. Energy Mater.*, 2022, **12**, 2104021.

18 S. Zhang, X. Zhuang, X. Du, X. Zhang, J. Li, G. Xu, Z. Ren, Z. Cui, L. Huang, S. Wang, F. Sun, L. Qiao, S. Dong and G. Cui, *Adv. Mater.*, 2023, **35**, e2301312.

19 Y. Cheng, Z. Wang, J. Chen, Y. Chen, X. Ke, D. Wu, Q. Zhang, Y. Zhu, X. Yang, M. Gu, Z. Guo and Z. Shi, *Angew. Chem., Int. Ed.*, 2023, **62**, e202305723.

20 Y. Feng, Y. Li, J. Lin, H. Wu, L. Zhu, X. Zhang, L. Zhang, C. F. Sun, M. Wu and Y. Wang, *Nat. Commun.*, 2023, **14**, 3639.

21 J. Pokharel, A. Cresce, B. Pant, M. Y. Yang, A. Gurung, W. He, A. Baniya, B. S. Lamsal, Z. Yang, S. Gent, X. Xian, Y. Cao, W. A. Goddard, 3rd, K. Xu and Y. Zhou, *Nat. Commun.*, 2024, **15**, 3085.

22 J. Zheng, P. Yan, D. Mei, M. H. Engelhard, S. S. Cartmell, B. J. Polzin, C. Wang, J. G. Zhang and W. Xu, *Adv. Energy Mater.*, 2016, **6**, 1502151.

23 Q. Li, S. Tan, L. Li, Y. Lu and Y. He, *Sci. Adv.*, 2017, **3**, e1701246.

2632 | *Energy Environ. Sci.*, 2025, **18**, 2622–2633

This journal is © The Royal Society of Chemistry 2025

24 X. B. Cheng, T. Z. Hou, R. Zhang, H. J. Peng, C. Z. Zhao, J. Q. Huang and Q. Zhang, *Adv. Mater.*, 2016, **28**, 2888.

25 H. Fan, Q. Dong, C. Gao, B. Hong and Y. Lai, *Mater. Lett.*, 2019, **234**, 69.

26 Q. Chen, Y. Wei, X. Zhang, Z. Yang, F. Wang, W. Liu, J. Zuo, X. Gu, Y. Yao, X. Wang, F. Zhao, S. Yang and Y. Gong, *Adv. Energy Mater.*, 2022, **12**, 2200072.

27 L. Ruan, X. Qin, K. Lin, Z. Yang, Q. Cai, T. Li, F. Wu, F. Kang and B. Li, *Nano Res.*, 2022, **16**, 4917.

28 R. He, Y. Wang, C. Zhang, Z. Liu, P. He, X. Hong, R. Yu, Y. Zhao, J. Wu, L. Zhou and L. Mai, *Adv. Energy Mater.*, 2023, **13**, 2204075.

29 A. J. Louli, M. Genovese, R. Weber, S. G. Hames, E. R. Logan and J. R. Dahn, *J. Electrochem. Soc.*, 2019, **166**, A1291.

30 J. Xing, T. Chen, L. Yi, Z. Song, X. Chen, C. Wei, A. Zhou, H. Li and J. Li, *Energy Storage Mater.*, 2023, **63**, 103067.

31 P. Albertus, S. Babinec, S. Litzelman and A. Newman, *Nat. Energy*, 2017, **3**, 16.

32 X. Zhang, X. Lin, P. Xu, R. Yuan, D. Gupta, R. Rupp, G. Barozzino-Consiglio, H. Xu, Q. Dong and A. Vlad, *J. Power Sources*, 2022, **541**, 231644.

33 J. Cao, Y. Shi, A. Gao, G. Du, M. Dilxat, Y. Zhang, M. Cai, G. Qian, X. Lu, F. Xie, Y. Sun and X. Lu, *Nat. Commun.*, 2024, **15**, 1354.

34 B. Zhou, A. Bonakdarpour, I. Stoševski, B. Fang and D. P. Wilkinson, *Prog. Mater. Sci.*, 2022, **130**, 100996.

35 J. Chen, J. Xiang, X. Chen, L. Yuan, Z. Li and Y. Huang, *Energy Storage Mater.*, 2020, **30**, 179.

36 D. Tang, L. Yuan, Y. Liao, W. Jin, J. Chen, Z. Cheng, X. Li, B. He, Z. Li and Y. Huang, *Sci. China Mater.*, 2022, **65**, 2385.

37 A. Fu, C. Wang, J. Peng, M. Su, F. Pei, J. Cui, X. Fang, J. F. Li and N. Zheng, *Adv. Funct. Mater.*, 2021, **31**, 2009805.

38 Y. Liu, D. Gao, H. Xiang, X. Feng and Y. Yu, *Energy Fuels*, 2021, **35**, 12921.

39 Y. Wang, Z. Zhao, J. Zhong, T. Wang, L. Wang, H. Xu, J. Cao, J. Li, G. Zhang, H. Fei and J. Zhu, *Energy Environ. Mater.*, 2021, **5**, 969.

40 L. Liu and J. Wang, *Nano Lett.*, 2023, **23**, 10251.

41 S. J. Zhang, Z. G. Gao, W. W. Wang, Y. Q. Lu, Y. P. Deng, J. H. You, J. T. Li, Y. Zhou, L. Huang, X. D. Zhou and S. G. Sun, *Small*, 2018, **14**, 1801054.

42 Y. Jung, S. Park, J. K. Kim, M. Kim and B. Kang, *Adv. Funct. Mater.*, 2022, **32**, 2109759.

43 K. H. Chen, A. J. Sanchez, E. Kazyak, A. L. Davis and N. P. Dasgupta, *Adv. Energy Mater.*, 2019, **9**, 1802534.

44 G. Y. Zheng, S. W. Lee, Z. Liang, H. W. Lee, K. Yan, H. B. Yao, H. T. Wang, W. Y. Li, S. Chu and Y. Cui, *Nat. Nanotechnol.*, 2014, **9**, 618.

45 X. C. Wang, Y. F. He, S. B. Tu, L. Fu, Z. H. Chen, S. Y. Liu, Z. Cai, L. Wang, X. M. He and Y. M. Sun, *Energy Storage Mater.*, 2022, **49**, 135.

46 S. Liu, X. Y. Zhang, R. S. Li, L. B. Gao and J. Y. Luo, *Energy Storage Mater.*, 2018, **14**, 143.

47 J. Seo, J. Lim, H. Chang, J. Lee, J. Woo, I. Jung, Y. Kim, B. Kim, J. Moon and H. Lee, *Small*, 2024, **20**, 2402988.

48 D. Q. He, W. J. Cui, X. B. Liao, X. F. Xie, M. H. Mao, X. H. Sang, P. C. Zhai, Y. Zhao, Y. H. Huang and W. Y. Zhao, *Adv. Sci.*, 2022, **9**, 2105656.

49 M. Gao, Q. Dong, M. Yao, X. Wang, J. Li, W. Zhang, H. Huang, H. Guo, Z. Sun, Q. Chen, X. Han and W. Hu, *Adv. Funct. Mater.*, 2024, **34**, 2401442.

50 S. Qian, C. Xing, M. Zheng, Z. Su, H. Chen, Z. Wu, C. Lai and S. Zhang, *Adv. Energy Mater.*, 2022, **12**, 2103480.

51 X. S. Xiong, W. Q. Yan, Y. S. Zhu, L. L. Liu, L. J. Fu, Y. H. Chen, N. F. Yu, Y. P. Wu, B. Wang and R. Xiao, *Adv. Energy Mater.*, 2022, **12**, 2103112.

52 Y. X. Song, W. Y. Lu, Y. J. Chen, H. Yang, C. Wu, W. F. Wei, L. B. Chen and X. P. Ouyang, *Rare Met.*, 2021, **41**, 1255.

53 Q. Chen, T. Zhang, Z. Hou, W. Zhuang, Z. Sun, Y. Jiang and L. Huang, *Chem. Eng. J.*, 2022, **433**, 133270.

54 Q. Dong, W. Zhang, M. Gao, S. Zhang, Y. Liu, Z. Sun, Q. Chen, J. Wang, X. Han and W. Hu, *Chem. Eng. J.*, 2023, **471**, 144483.

55 X. Q. Zhang, X. Chen, R. Xu, X. B. Cheng, H. J. Peng, R. Zhang, J. Q. Huang and Q. Zhang, *Angew. Chem., Int. Ed.*, 2017, **56**, 14207.

56 J. Cai, L. Wang, Q. Huang, W. Yu, C. Xie and Z. Zheng, *Adv. Energy Mater.*, 2024, **14**, 2303088.

57 J. Cao, W. Chen, A. Gao, G. Du, D. Muhtar, G. Qian, X. Lu, F. Xie, Y. Sun and X. Lu, *Angew. Chem., Int. Ed.*, 2024, e202413065.

58 Z. Yu, D. G. Mackanic, W. Michaels, M. Lee, A. Pei, D. Feng, Q. Zhang, Y. Tsao, C. V. Amanchukwu, X. Yan, H. Wang, S. Chen, K. Liu, J. Kang, J. Qin, Y. Cui and Z. Bao, *Joule*, 2019, **3**, 2761.

59 S. Liu, X. Zhang, R. Li, L. Gao and J. Luo, *Energy Storage Mater.*, 2018, **14**, 143.

60 J. Chen, G. Liu, X. Han, H. Wu, T. Hu, Y. Huang, S. Zhang, Y. Wang, Z. Shi, Y. Zhang, L. Shi, Y. Ma, H. N. Alshareef and J. Zhao, *ACS Nano*, 2024, **18**, 13662–13674.

61 D. Yang, X. Wu, L. He, H. Zhao, Y. Wang, Z. Zhang, J. Qiu, X. Chen and Y. Wei, *Nano Lett.*, 2023, **23**, 11152.

62 Y. S. Feng, Y. N. Li, P. Wang, Z. P. Guo, F. F. Cao and H. Ye, *Angew. Chem., Int. Ed.*, 2023, **62**, e202310132.

63 X. Li, Y. Su, Y. Qin, F. Huang, S. Mei, Y. He, C. Peng, L. Ding, Y. Zhang, Y. Peng and Z. Deng, *Adv. Mater.*, 2023, **35**, e2303489.

64 X. Zhan, M. Li, X. Zhao, Y. Wang, S. Li, W. Wang, J. Lin, Z.-A. Nan, J. Yan, Z. Sun, H. Liu, F. Wang, J. Wan, J. Liu, Q. Zhang and L. Zhang, *Nat. Commun.*, 2024, **15**, 1056.

65 Y. Gu, H. Y. Xu, X. G. Zhang, W. W. Wang, J. W. He, S. Tang, J. W. Yan, D. Y. Wu, M. S. Zheng, Q. F. Dong and B. W. Mao, *Angew. Chem., Int. Ed.*, 2019, **58**, 3092.

66 D. Zhang, A. Dai, M. Wu, K. Shen, T. Xiao, G. Y. Hou, J. Lu and Y. P. Tang, *ACS Energy Lett.*, 2020, **5**, 180.

This journal is © The Royal Society of Chemistry 2025

*Energy Environ. Sci.*, 2025, **18**, 2622–2633 | **2633**